CDF note 10788

The Search For New Physics in the Exclusive $\gamma_{\mathbf{delayed}} + \not\!\!E_{\mathbf{T}}$ Signature in $p\bar{p}$ Collisions at $\sqrt{s} = 1.96$ TeV

The CDF Collaboration
URL http://www-cdf.fnal.gov
(Dated: October 5, 2012)

We present the first model-independent search for massive, long-lived particles that decay to photons in the exclusive photon and missing energy final state in $p\bar{p}$ collisions at $\sqrt{s} = 1.96$ TeV. A sample of 6.3 fb^{-1} of integrated luminosity collected by the CDF II detector is analyzed. Candidate events are selected based on the photon having a delayed arrival-time in the detector. We observe 322 events on a background of 286 ± 24 events from collision and non-collision sources. We quantify this modest excess as 1.2 standard deviations.

I. INTRODUCTION

We present the first model-independent search for massive, long-lived particles that decay to photons in the exclusive photon and missing energy final state in $p\bar{p}$ collisions at $\sqrt{s} = 1.96$ TeV. A sample of 6.3 fb^{-1} of integrated luminosity collected by the CDF II detector is analyzed. Candidate events are selected based on the photon having a delayed arrival-time in the detector. This work follows many of the predictions described in GMSB phenomenology papers [1, 2], and updates many of the methods dscribed in an inclusive $\gamma_{\rm delayed} + \not\!\!E_{\rm T} +$jets study at CDF using just 0.57 fb^{-1} of integrated luminosity [3, 4], but in the exclusive $\gamma + \not\!\!E_{\rm T}$ final state.

A. Motivation

The standard model (SM) of particle physics is known to be an incomplete theory, despite being one of the cornerstones of our current understanding of the physical world. Naturally, an extension must be added to the SM to account for the phenomena we currently observe in the universe for which there is no known explanation. While there are many models to search for, and model-specific searches should be also done, we can use models to guide model-independent searches.

One such plausible extension is known as Supersymmetry (SUSY), where for every fermionic particle there exists a bosonic partner, and vice versa. These supersymmetric partner particles are denoted "sparticles." Gauge Mediated Supersymmetry Breaking(GMSB) models can produce a heavy next-to-lightest neutralino ($\tilde{\chi}_1^0$) that decays to a photon (γ) and gravitino ($\tilde{G}$), which does not interact with the detector, thereby providing a $\gamma + \not\!\!E_{\rm T}$ final state [1–4]. There are many plausible models of GMSB production and decay accessible at the Tevatron in Run II, some of which are summarized in Tab. I. The most commonly discussed and searched for GMSB models are the SPS-8-type scenarios [5]. Just above the current Tevatron exclusion limits, the dominant sparticle production mode at the Tevatron is $\tilde{\chi}_1^{\pm}\tilde{\chi}_2^0$ and $\tilde{\chi}_1^+\tilde{\chi}_1^-$. Each will decay to a photon and gravitino, as well as other high energy particles. Thus, the final state is two photons, $\not\!\!E_{\rm T}$, and other large-energy deposits, if the lifetime is short, but a single photon plus $\not\!\!E_{\rm T} +$jets, where the photon arrives at the detector later than expected, $\gamma_{\rm delayed}$, if the $\tilde{\chi}_1^0$ lifetime is long [1]. These models have been searched for at the Tevatron with no evidence for new physics [3, 4, 6], as well as in complementary searches at LEP and the LHC [7–13].

Model	$\tau_{\tilde{\chi}_1^0} \lessapprox 1$**ns**	$1 < \tau_{\tilde{\chi}_1^0} < 50$ **ns**
SPS-8 GMSB Production	$\gamma\gamma + \not\!\!E_{\rm T} + H_T$	$\gamma_{\rm delayed} + \not\!\!E_{\rm T}$+ jets
Higgs-Type Production	Exclusive $\gamma\gamma + \not\!\!E_{\rm T}$	Exclusive $\gamma_{\rm delayed} + \not\!\!E_{\rm T}$

TABLE I: A breakdown of GMSB searches by lifetime as well as production mode for the Tevatron. SPS-8 refers to the Snowmass Points and Slopes model for benchmark points and parameters [5] and is dominated by $\chi_1^+\chi_1^-$ and $\chi_1^{\pm}\chi_2^0$ pair production. In the Light Neutralino and Gravitino (LNG) scenario [2, 14], models where only the $\tilde{\chi}_1^0$ and $\tilde{G}$ have masses low enough to be preferentially produced in collider experiments are produced through a Higgs if the masses are kinematically favorable.

In this analysis we are guided by new predictions from important GMSB models where only the $\tilde{\chi}_1^0$ and $\tilde{G}$ have masses accessible in $p\bar{p}$ collisions at $\sqrt{s} = 1.96$ TeV [1, 2, 14]. These scenarios are known as the Light Neutralino and Gravitino (LNG) scenario [2, 14]. In such cases, the dominant production mechanisms are neutralino pairs via the off-shell direct production of a Z boson ($Z \to \tilde{\chi}_1^0\tilde{\chi}_1^0 \to \gamma\tilde{G}\gamma\tilde{G}$) or via production from a Higgs boson (see Eqn. 1 and Fig. 1), if the masses and branching ratios are favorable.

$$gg \to h^0 \to \tilde{\chi}_1^0\tilde{\chi}_1^0 \to \gamma\tilde{G}\gamma\tilde{G} \tag{1}$$

Since the dominant production cross section of the Higgs boson is not in association with other particles, we consider exclusive final states. No limits have yet been set on long or short lifetimes of the production mechanism in the LNG scenario, however short lifetime new physics should have appeared in the exclusive $\gamma\gamma + \not\!\!E_{\rm T}$, but a previous search found no evidence of new physics [15]. Since there is no evidence for short lifetime production, we consider long lifetimes.

In this document we summarize a model-independent search [16, 17], based on the prediction for heavy, long-lived particles that decay to $\gamma + \not\!\!E_{\rm T}$, in the exclusive $\gamma_{\rm delayed} + \not\!\!E_{\rm T}$ final state using 6.3 fb^{-1} of integrated luminosity collected by Run II of the Collider Detector at Fermilab (CDF). As such, the analysis presented here is conducted as a general search for new physics and we do not attempt to set limits on any particular model. We follow and significantly update many of the methods described in an inclusive $\gamma_{\rm delayed} + \not\!\!E_{\rm T} +$ jets study at CDF using just

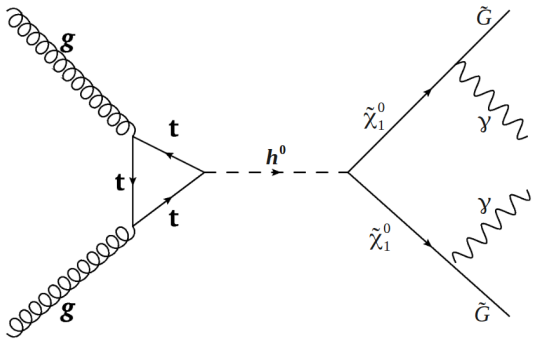

FIG. 1: In the Light Neutralino and Gravitino GMSB models, only the $\tilde{\chi}_1^0$ and $\tilde{G}$ have masses that are accessible at Tevatron energies. If the masses are favorable, sparticles are produced through the production and decay of a Higgs boson. These models suggest exclusive $\gamma\gamma + \not\!\!E_{\rm T}$ if the neutralino has a short lifetime or $\gamma_{\rm delayed} + \not\!\!E_{\rm T}$ if the lifetime is long, on the order of 5 ns.

0.57 fb^{-1} of integrated luminosity [3, 4] and a second independent search in exclusive $\gamma + \not\!\!E_{\rm T}$ [18] which focused on a search for large extra dimensions.

B. CDF II Detector

Detailed descriptions of the CDF II detector can be found elsewhere [19], but we briefly describe aspects of the detector relevant to this analysis. Since CDF II is a cylindrically symmetric, we utilize the standard CDF coordinate system [20]. The detector itself is a typical modern detector composed of a silicon microstrip tracking system ("silicon vertex detector" or SVX), a 3.1 meter long drift chamber ("central outer tracker" or COT) that measures the times and trajectories of charged particles, a calorimeter system, and a muon tracking system. For well-measured tracks used in this analysis, the resolution on the extrapolated time and position along the beam line is 0.22 ns and 0.24 cm, respectively [4]. Surrounding the tracking chambers is the projective calorimeter system, comprised of separate electromagnetic and hadronic compartments used to identify photons and measure the $\not\!\!E_{\rm T}$ in the event. The electromagnetic calorimeter system was outfitted with an electromagnetic timing system which reports the arrival-time of electromagnetic energy deposits (e.g. photons and electrons) with a resolution of 0.600 ± 0.010 ns [21]. Our custom spacetime vertexing procedure looks for clusters of well-measured tracks in space and time, and any vertex-candidate must have at least three tracks converging within a parameter space window of 1.5 ns $\times$ 1.5 cm.

C. Photon Timing for $\gamma_{\rm delayed}$ Searches

Prompt photons occur from a $p\bar{p}$ collision at some initial coordinate $(\vec{x}_{\rm i}, t_{\rm i})$ as measured by the tracking chambers and are subsequently recorded by the calorimeter system at final coordinate $(\vec{x}_{\rm f}, t_{\rm f})$ as shown in Fig. 2. New physics, such as the possibility of heavy, long-lived neutralinos, can manifest itself as an intermediate particle state which decays to a photon that is then detected by the calorimeter as shown in Fig. 2(b). Because the latter case involves a less direct path from $(\vec{x}_{\rm i}, t_{\rm i})$ to $(\vec{x}_{\rm f}, t_{\rm f})$ than that of a prompt photon, the total time-of-flight from the collision point is longer, making the arrival-time in the calorimeter relatively later; this is why we call the photon a delayed photon. A useful variable for measuring the amount of delay of a photon has been used for many years [3, 4, 21] and is defined as the time of arrival, minus the time of production minus the expected time-of-flight (TOF) from the collision point to the calorimeter point. This is written as:

$$t_{\rm corr} = (t_{\rm f} - t_{\rm i}) - \frac{|\vec{x}_{\rm f} - \vec{x}_{\rm i}|}{c}, \tag{2}$$

or

$$t_{\rm corr} = (t_{\rm f} - t_{\rm i}) - {\rm TOF}, \tag{3}$$

where

$$\mathrm{TOF} = \frac{|\vec{x}_\mathrm{f} - \vec{x}_\mathrm{i}|}{c}. \quad (4)$$

In principle, the shape of the distribution of t_{corr} of photons produced promptly in a $p\bar{p}$ interaction and that traverse unobstructed from the vertex at $(\vec{x}_\mathrm{i}, t_\mathrm{i})$ to the detector at $(\vec{x}_\mathrm{f}, t_\mathrm{f})$, is Gaussian with a mean of 0.0 ns and an RMS corresponding to the combined vertexing and calorimeter resolution of 0.65 ± 0.05 ns [21], assuming the correct vertex was selected. An example of signal of $\tilde{\chi}_1^0 \to \gamma + \tilde{G}$ would show up as an exponential for positive times and would be well separated from SM sources when we define a signal region for this analysis as $2 < t_{\mathrm{corr}} < 7$ ns [1, 3, 4].

Since SM events with a correctly identified vertex are readily separated from new physics, the dominant backgrounds at large values of t_{corr} are dominated by a combination of SM sources where the wrong vertex is selected and used in Eqn. 3, and from cosmic ray backgrounds. Both are listed in Table II. Since the collision that produces $\gamma + \not\!\!E_\mathrm{T}$ does not always reconstruct a vertex and because collider events can produce more than one $p\bar{p}$ collision which produces detectable physics, the correct vertex is not always selected or available as shown in Fig. 2(a). The timing shape of the t_{corr} distribution where the wrong vertex is selected, known as wrong-vertex events as will be described in detail later, is given by a Gaussian, but with an RMS of 2.0 ns and a mean that is not centered at zero. The rate and mean of this distribution from the sum of the collision backgrounds will be determined using data-driven methods.

Standard Model Collision Sources
$W \to e\nu \to \gamma_{\mathrm{fake}} + \not\!\!E_\mathrm{T}$
$\gamma + \mathrm{jet} \to \gamma + \mathrm{jet}_{\mathrm{lost}} \to \gamma + \not\!\!E_{\mathrm{T\,fake}}$
$W\gamma \to l\nu\gamma \to \gamma + l_{\mathrm{lost}} + \not\!\!E_\mathrm{T}$
$W \to \mu\nu \to \gamma_{\mathrm{fake}} + \not\!\!E_\mathrm{T}$
$W \to \tau\nu \to \gamma_{\mathrm{fake}} + \not\!\!E_\mathrm{T}$
$Z\gamma \to \nu\nu\gamma \to \gamma + \not\!\!E_\mathrm{T}$
Non-Collision Sources
Cosmics
Beam Halo
Satellite Bunches

TABLE II: Standard model and non-collision backgrounds for the exclusive $\gamma + \not\!\!E_\mathrm{T}$ search.

While beam-halo [3, 4, 18] and satellite bunch collisions can produce $\gamma + \not\!\!E_\mathrm{T}$ events in the signal region, the dominant non-collision background are cosmic rays. Cosmic rays produce a $\gamma + \not\!\!E_\mathrm{T}$ signature that is uncorrelated to the timing of the Tevatron beam collisions, so they appear as a uniform distribution over t_{corr}, and can populate the signal region. However, data-driven techniques are readily used to determine the expected rate in the signal region. Figure 2(c) shows a toy of the expected backgrounds and signal shape expected for this analysis. The expected background shape is well described by the sum of two Gaussian distributions from collision events and a uniform distribution from cosmic rays.

D. Overview of the Analysis

While the backgrounds are well described by the seven parameters which define the aforementioned double-Gaussian plus uniform distribution (three parameters describe each Gaussian distribution and one describes the uniform distribution), the crux of this analysis is determining the values of each. Each parameter will be obtained in a data-driven manner from several sideband regions. Most of the parameters for the two Gaussian distributions can be found from the "collision sideband" window of $-7 < t_{\mathrm{corr}} < 2$ ns, but this will be insufficient for precisely determining the mean of the wrong-vertex Gaussian distribution, $\langle t_{\mathrm{corr}}^{\mathrm{WV}} \rangle$. This last parameter can be determined from the sample of events that are topologically identical to the exclusive $\gamma + \not\!\!E_\mathrm{T}$ events, but have zero identified vertices. This sample is known as the "no-vertex sideband" sample. We will demonstrate this with a variety of data and MC control samples. The uniform distribution that describes the cosmic ray background contribution can be obtained from a pure cosmics sample created using events far from the collision time, $20 < t_{\mathrm{corr}} < 80$ ns. A multibinned, simultaneous, maximum likelihood fit to all sideband regions will provide the background expectation in the exclusive signal timing region.

In Section II we describe the criteria used to create our $\gamma + \not\!\!E_\mathrm{T}$ samples. In Section III we describe the backgrounds, both SM and non-collision, that can create (or mimic) our $\gamma + \not\!\!E_\mathrm{T}$ signature. In Section IV we describe our data-driven background estimation method and our expectations. Finally, in Section V we present the result and our conclusions.

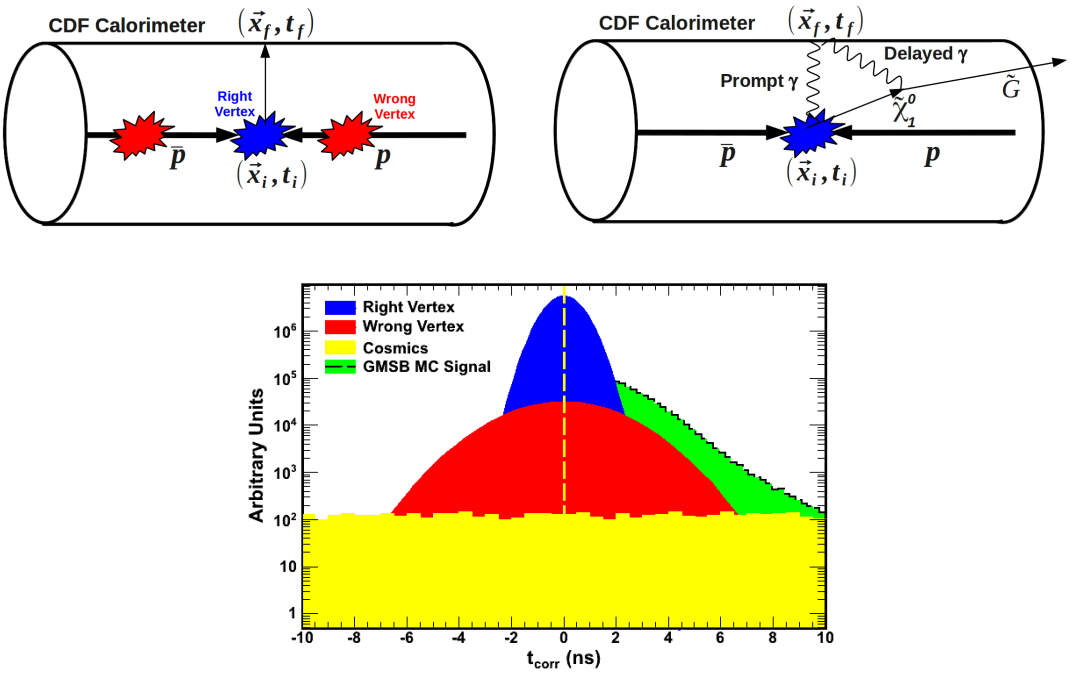

FIG. 2: (a): Prompt photons have an arrival time consistent with traveling from the collision point to the calorimeter at the speed of light. However, multiple collisions can occur in each event, and sometimes the right vertex is not reconstructed. The selection of the wrong vertex can significantly affect the timing distribution for promptly produced photons. (b): Photons coming from the decay of heavy, long-lived neutralinos come from a location displaced in space and time from the collision point so photons tend to arrive late relative to expectations from prompt photons. (c): A cartoon showing the expected timing distribution divided into components. Standard model backgrounds contribute right and wrong-vertex Gaussians and cosmics contribute a flat background. Signal from a long-lived neutralino would look approximately like a falling exponential smeared by the detector resolution for positive values of $t_{\rm corr}$.

II. EVENT SELECTION AND DATA SAMPLES

This analysis uses 6.3 fb^{-1} of integrated luminosity. The data are collected with online inclusive triggers which require a high-E_T EM cluster recorded by the calorimeter system along with high $\not\!\!E_{\rm T}$ (see Tab. III) as well as a set of other triggers to make the overall trigger efficiency effectively 100%. Offline, events are required to pass the photon identification requirements (see Tab. IV) and final event selection (see Tab. V).

Photons are identified using the standard CDF requirements [22], with a few caveats [3, 4]. Most notably, the $\chi^2_{\rm CES}$ cut is removed as it has been shown to be inefficient for photons that don't originate directly from the beamline and a PMT asymmetry cut is added to reduce the possibility of PMT spikes For the purpose of removing cosmic rays, new minimum CES energy and hadronic energy cuts were developed for this analysis and this will be described in more detail in Sec. III A. To minimize the SM backgrounds, especially $W \to e\nu \to \gamma_{\rm fake} + \not\!\!E_{\rm T}$, the photon $E_{\rm T}$ and $\not\!\!E_{\rm T}$ are required to have at least 45 GeV each. Lastly, the photon $E_{\rm T}$ and $\not\!\!E_{\rm T}$ values are computed from $z = 0$ cm rather than the selected collision vertex to be less biased when the wrong vertex is selected. This choice will be discussed in Section III C 1.

In addition to reducing electron and fake backgrounds from SM collisions, we remove non-collision events with a set of cuts. The standard beam halo and cosmics removal techniques have been used for many years and are described elsewhere [3, 4, 18, 23].

Since we want to reject events from $W\gamma \to l\nu\gamma$ and γ + jets we consider the exclusive $\gamma + \not\!\!E_{\rm T}$ final state. In particular, we veto any event based on the presence of a high $p_{\rm T}$ track or extra jets. Specifically, events with extra energy deposits in the calorimeter ($E_T > 15$ GeV) or events with a high-p_T ($p_T > 10$ GeV) track are removed from the event sample.

We next place three additional requirements on our exclusive $\gamma + \not\!\!E_{\rm T}$ sample to reduce the contribution from SM sources with large values of $t_{\rm corr}$. These will be described in more detail in Section III but we include them here for completeness. Since the selection of the wrong vertex produces events with large values of $t_{\rm corr}$, we use two types of vertexing algorithms. The first is the standard vertexing algorithm that clusters tracks in z [24, 25]. This is very efficient for finding collisions, even at large z, but does not separate between two collisions that occur close in space, but not in time. This algorithm will be used to veto SM events that are produced at large values of $|z|$ along the beamline and are produce a badly mismeasured value of $t_{\rm corr}$ in this analysis. To get a good measurement of a single collision in both space and time for use in Eqn. 3, we use a SpaceTime vertexing algorithm that does clustering in both space and time to help separate collisions in our measurement of $t_{\rm corr}$ [3, 4, 21]. The sum of the $p_{\rm T}$ of all tracks in a SpaceTime vertex must be greater than 5 GeV, and must be no more than 60 cm from the center of the detector along the beamline ($|z| < 60$ cm).

Finally, since $W \to e\nu \to \gamma_{\rm fake} + \not\!\!E_{\rm T}$ events are a large background and produce some of the largest arrival-times, we have added a new electron rejection requirement. Events that physically originate as $e + \not\!\!E_{\rm T}$ can be identified as $\gamma_{\rm fake} + \not\!\!E_{\rm T}$ and pass all the standard photon identification requirements if the electron bremmstrahlung's a photon via interaction with the detector apparatus. Such photons are also predisposed to have a late arrival-time relative to prompt photons, so a new loose electron rejection is employed to reduce this background (see Section III C 3).

The event count of the data sample for each step of these analysis cuts are summarized in Tab. VI. We note that in the last line we have separated our subsample of $\gamma + \not\!\!E_{\rm T}$ events into a sample with at least one identified SpaceTime vertex and those that have no reconstructed vertex for reasons that will be described in more detail in Section IV. There is a total of $5,421$ events with a good SpaceTime vertex. The final signal region is defined as 2 ns $< t_{\rm corr} <$ 7 ns.

At this point. we also note that we have six MC control samples corresponding to the entries of Tab. II as well as two data control samples for $e + \not\!\!E_{\rm T}$. The MC control samples correspond to all the known ways that SM collisions produce the $\gamma + \not\!\!E_{\rm T}$ final state and are simulated using the PYTHIA [26, 27] and BAUR [28] MC generators and the full CDF Detector simulation package [29]. The $e + \not\!\!E_{\rm T}$ sample is chosen because electrons mimic photons in the detector if we simply remove the electron track from the vertexing, but allow it to tell us if the algorithms have picked the correct vertex. This will allow us to test our analysis methods as well as confirm that the MC samples well-represent what is observed in the detector. The electron data for our control sample is selected according to the requirements in Tabs. VII and VIII.

Object Type	Trigger		
	Level 1	**Level 2**	**Level 3**
WNOTRACK			
EM cluster	≥ 1 Central EM cluster $E_T^0 > 8$ GeV $\frac{E_{\rm Had}}{E_{\rm EM}} < 0.125$	$\lvert\eta\rvert < 1.1$ $E_T^0 > 20$ GeV $E_T^{\rm SeedTower} > 8$ GeV	≥ 1 EM cluster $E_T^0 > 25$ GeV $\frac{E_{\rm Had}}{E_{\rm EM}} < 0.125$
Missing E_T	$\not\!\!E_{\rm T}^0 > 15$ GeV $\Sigma E_T^0 > 1$ GeV		$\not\!\!E_{\rm T}^0 > 25$ GeV
WNOTRACK NO L2			
EM cluster	≥ 1 Central EM cluster $E_T^0 > 8$ GeV $\frac{E_{\rm Had}}{E_{\rm EM}} < 0.125$		$\frac{E_{\rm Had}}{E_{\rm EM}} < 0.125$
Missing E_T	$\not\!\!E_{\rm T}^0 > 15$ GeV		$\not\!\!E_{\rm T}^0 > 25$ GeV
SUPERPHOTON70			
EM cluster	≥ 1 Central EM cluster $E_T^0 > 10$ GeV	$\lvert\eta\rvert < 1.1$ $E_T^0 > 70$ GeV $E_T^{\rm SeedTower} > 8$ GeV	≥ 1 EM cluster $E_T^0 > 70$ GeV $\frac{E_{\rm Had}}{E_{\rm EM}} < 0.2$
SUPERPHOTON70 L2			
EM cluster	≥ 1 Central EM cluster $E_T^0 > 20$ GeV $\frac{E_{\rm Had}}{E_{\rm EM}} < 0.125$	≥ 1 Central EM cluster $E_T^0 > 70$ GeV $0.0 \leq \lvert\eta\rvert \leq 3.6$ $\frac{E_{\rm Had}}{E_{\rm EM}} < 0.2$	
PHOTON25ISO			
EM cluster	≥ 1 Central EM cluster $E_T^0 > 8$ GeV $\frac{E_{\rm Had}}{E_{\rm EM}} < 0.125$	$\lvert\eta\rvert < 1.1$ $E_T > 21$ GeV $E_T^{\rm SeedTower} > 8$ GeV $E_T^{\rm ISO} < 3$ GeV $\frac{E_{\rm Had}}{E_{\rm EM}} < 0.125$	≥ 1 EM cluster $E_T^0 > 25$ GeV $\rm Iso^{Total} < 2.0$ $\chi^2 < 20$ $\frac{E_{\rm Had}}{E_{\rm EM}} < 0.055$
ELECTRON70			
EM cluster	≥ 1 Central EM Cluster $E_T^0 > 20$ GeV	≥ 1 Central EM Cluster $E_T^0 > 70$ GeV $0.0 \leq \lvert\eta\rvert \leq 3.6$	$\frac{E_{\rm Had}}{E_{\rm EM}} < 0.2$
ULTRAPHOTON50			
EM cluster	≥ 1 Central EM Cluster $E_T^0 > 12$ GeV $\frac{E_{\rm Had}}{E_{\rm EM}} < 0.125$	≥ 1 Central EM Cluster $E_T^0 > 50$ GeV $0.0 \leq \lvert\eta\rvert \leq 3.6$ $\frac{E_{\rm Had}}{E_{\rm EM}} < 0.125$	$\frac{E_{\rm Had}}{E_{\rm EM}} < 0.125$

TABLE III: Online event selection for the W_NOTRACK triggers, as well as a list of additional triggers we allow using the logical *or* of all triggers.

Quantity	Selection Cut
EM cluster E_T^0	1 cluster with $E_T^0 > 30$ GeV
Fiducial	$\lvert X_{\rm CES}\rvert < 21$ cm and $9 < \lvert Z_{\rm CES}\rvert < 230$ cm
Hadronic fraction	$\frac{E_{\rm Had}}{E_{\rm EM}} < 0.125$ $E_{\rm Had} > -0.3 + 0.008 \cdot E_{\rm T}^0$*
Energy isolation	$E^{\rm iso}_{\rm cone\ 0.4} < 2.0 + 0.02 \cdot (E_T^0 - 20.0)$
1st CES cluster energy	CES $E > 10$ GeV* CES $E/E > 0.2$*
2nd CES cluster energy (if one exists)	CES $E^{\rm 2nd} < 2.4 + 0.01 \cdot E_T^0$
PMT spike rejection	$A_{\rm PMT} = \frac{\lvert E_{\rm PMT1} - E_{\rm PMT2}\rvert}{E_{\rm PMT1} + E_{\rm PMT2}} < 0.6$*
Track Multiplicity	Number of N3D tracks either 0 or 1
Track P_T	If $N3D = 1 \rightarrow P_T < 1.0 + 0.005 \cdot E_T^0$

TABLE IV: The photon identification criteria. Note that these are standard requirements for high E_T photons [22], with the following exceptions (marked with a * on the above table) described in [4] and [23]: the standard $\chi^2_{\rm CES}$ cut is removed, we add a PMT asymmetry cut to reject PMT spikes, and three new cuts on $E_{\rm Had}$, CES E and CES E/E, are added to reject cosmics. Note that many of these variables (E_T^0, energy isolation, 2nd CES energy and track P_T requirement) are calculated using the photon algorithm run with $z = 0$ rather than using z of the primary vertex as they will not be well defined or biased for events where the wrong vertex is selected.

Quantity	Selection Cut
Trigger (applied to data only)	`WNOTRACK` or other triggers in Tab. III
Good photon passing the ID cuts in Table IV	$E_T > 45$ GeV
$\not\!\!E_{\rm T}$ $(z = 0)$	> 45 GeV
Standard Beam Halo Rejection	Reject event if the cluster has 9 or more hits in the same wedge, or has 2 or more hadronic tower hits associated
Standard Cosmic Ray Rejection	$\Delta\phi(\gamma, \text{closest muon stub}) > 30$ degrees
Track veto	$P_T > 10$ GeV NCotAxSeg(5)≥ 2 $\frac{\text{COT \# HitsTotal}}{\text{COT LastLayer + 1}} > 0.6$
Veto on any jet not identified as the leading photon	$E_T > 15$ GeV
Large standard vertex $\lvert z\rvert$ veto	$\lvert z\rvert < 60.0$ cm for all identified standard vertices
Electron rejection veto	$\Delta R_{\rm pull} > 5.0$
Vertex selection	Require at least one spacetime vertex with: $\Sigma P_T > 5.0$ GeV $\lvert Z_0\rvert < 60.0$ cm $N_{\rm Tracks} \geq 3$

TABLE V: The set of requirements to create the various exclusive $\gamma + \not\!\!E_{\rm T}$ datasets.

Requirement	Number of Events
Central photon with $E_T^0 > 45$ GeV, $\not\!\!E_{\rm T}^0 > 45$ GeV and passing trigger requirements	38,291
Beam halo veto	36,764
Cosmics veto	24,462
Track veto	16,831
Jet veto	12,708
Large $\lvert Z\rvert$ vertex veto	11,702
$e \rightarrow \gamma_{\rm Fake}$ veto	10,363
Good vertex events/no vertex events	5,421/4,942

TABLE VI: Event reduction table for the exclusive $\gamma + \not\!\!E_{\rm T}$ search. The last selection requirement breaks the events into two samples: 1) Events that do have a reconstructed SpaceTime vertex and 2) events that do not have a good SpaceTime vertex ("no vertex sample"). The sample of events that do have a reconstructed vertex are the events on which we perform our search for $\gamma_{\rm delayed} + \not\!\!E_{\rm T}$ while the "no vertex sample" is used to estimate $\langle t^0_{\rm corr}\rangle$.

Quantity	**Selection Cut**
EM cluster E_T^0	1 cluster with $E_T^0 > 45$ GeV
Fiducial	$\lvert X_{\rm CES}\rvert < 21$ cm and $9 < \lvert Z_{\rm CES}\rvert < 230$ cm
Hadronic fraction	$\frac{E_{\rm Had}}{E_{\rm EM}} < 0.055 + 0.00045 \cdot E_{\rm EM}$
Energy isolation	$E^{\rm iso}_{\rm cone\ 0.4} < 0.1 \cdot E_T^{\rm EM}$
$L_{\rm shr}$	< 0.2
Track P_T and E/P	Track $P_T > 50$ GeV, if $P_T < 50$ GeV, require $E/P < 2$

TABLE VII: The electron selection requirements. Note that these are standard electron requirements [30], with the exception of $\chi^2_{\rm CES}$ cut, which has been removed to make it consistent with the photon ID cuts, as well as the $|\Delta x|$ and $|\Delta z|$ requirements (which are between the CES cluster variables and the extrapolated track variables).

Quantity	**Selection Cut**
Trigger (applied to data only)	`WNOTRACK` or other triggers in Tab. III
Good electron passing the ID cuts in Table VII	$E_T > 45$ GeV
$\not\!\!E_{\rm T}$ $(z = 0)$	> 45 GeV
Standard Beam Halo Rejection	Reject event if the cluster has 9 or more hits in the same wedge, or has 2 or more hadronic tower hits associated
Standard Cosmic Ray Rejection	$\Delta\phi(e,$ closest muon stub$) > 30$ degrees
Track veto	$P_T > 10$ GeV NCotAxSeg(5)≥ 2 $\frac{\rm COT\ \#\ \ HitsTotal}{\rm COT\ LastLayer\ +\ 1} > 0.6$
Veto on any jet not identified as the leading electron	$E_T > 15$ GeV
Large standard vertex $\lvert z\rvert$ veto	$\lvert z\rvert < 60.0$ cm for all identified standard vertices
Electron rejection veto	$\Delta R_{\rm pull} > 5.0$
Vertex selection	Require at least one spacetime vertex with: $\Sigma P_T > 5.0$ GeV $\lvert Z_0\rvert < 60.0$ cm $N_{\rm Tracks} \geq 3$

TABLE VIII: The set of requirements to create the various exclusive $e + \not\!\!E_{\rm T}$ datasets.

III. BACKGROUNDS

The exclusive $\gamma + \not\!\!E_{\rm T}$ sample has both SM collision backgrounds and non-collision backgrounds that must be accounted for in modelling the expectations in the signal region. The collision SM backgrounds (see Tab. II) can be divided into two categories: events that have correctly chosen the SpaceTime vertex from which the photon originated (right vertex) and those that have chosen an incorrect vertex (wrong vertex). We will describe several effects that can cause photons in SM collisions to have large values of $t_{\rm corr}$. We will also describe the measures taken to minimize them, and describe the data-driven background estimation method used in this analysis in the next section. We begin with a description of the non-collision backgrounds for simplicity.

A. Non-Collision Backgrounds

Noncollision photon candidates are produced by cosmic rays and beam effects which have been studied and understood for many years [3, 4, 18]. The dominant background to the $\gamma + \not\!\!E_{\rm T}$ final state are from cosmic rays. Cosmic rays are reduced in our sample by the use of one standard requirement and two new requirements that are added as part of the photon ID; both were listed in Tables IV and V, but mentioned here in more detail. For our sample, photon candidates which are within a 30° azimuthal angle to hits in the muon chambers that are unassociated with tracks in the tracking chamber are rejected using the standard requirement [4], resulting in a 53% reduction in cosmic rays while retaining 72% of collision photons. Second, studies from electrons (which well model photon showers in the detector) and cosmic ray samples indicate that further reduction can be had with high efficiency since collision photons deposit greater quantites of energy in the hadronic calorimeter, behind the photon candidate, than do cosmic ray events. We require an E_T-dependent minimum quantity of hadronic energy: Hadronic $E > -0.30 + 0.008 \cdot E_T$. Since photons from cosmic ray candidates rarely shower in the calorimeter in the same way as photons from inside the detector, the independent measurement of the photon energy as measured at the shower max detector (CES) is much more likely to be lower than the full tower energy measurement. For this reason we require the energy measurement in CES to be a large fraction of the full shower energy measurement, in particular, we require CES E/Total $E > 0.2$. The distribution of these variables for cosmics and SM sources are illustrated in Fig. 3 and provide an excellent rejection against cosmics: 76% rejection of cosmics while remaining 92% efficient for collision photons after all event selection requirements.

Stray particles from the beam can potentially also impinge on the detector laterally and mimic a $\gamma + \not\!\!E_{\rm T}$ signature. This background is known as the Beam Halo background. While this was an important effect in previous delayed photon analyses [3, 4], it is now negligible in the final data sample after using the now-standard beam halo rejection requirements [18]. As we will see, events from cosmic rays are the dominant backgroind in our signal region after all the event selection requirements. However, they are easily modelled as a uniform distribution [3, 4] so additional rejection against them does not improve our sensitivity when compared with the dominant background uncertainties.

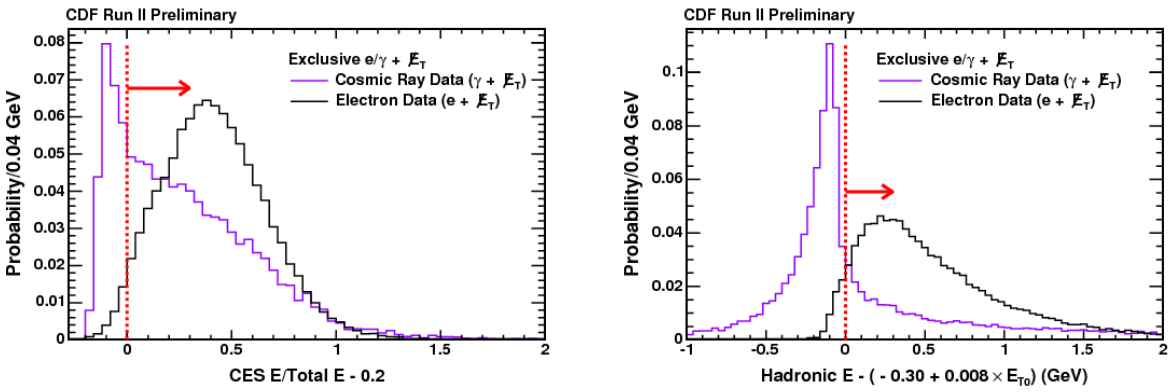

FIG. 3: (a): Hadronic energy cut for cosmic ray removal (b): CES energy cut for cosmic ray removal

B. Collision Backgrounds

Standard model contributions to the $\gamma + \not\!\!E_{\rm T}$ final state originate from interactions such as $\gamma +$ jets where a lost jet mimics $\not\!\!E_{\rm T}$, $Z\gamma \to \nu\nu\gamma$, $W \to l\nu$ where the lepton or an extraneous jet is misidentified as a photon, and $W\gamma \to l\nu\gamma$ where the lepton fails to be identified. The full list is given in Table II. To reject most of these backgrounds we require the exclusive final state. We can use our $e + \not\!\!E_{\rm T}$ sample described in Table VIII to simulate $\gamma + \not\!\!E_{\rm T}$ events if we ignore the electron track in the vertexing, but use the electron track to identify the righ vertex or the wrong vertex. The results are shown in Fig. 4. Our double Gaussian description does an excellent job of modeling the data, both for the individual backgrounds as well as the combined background. Note that we have allowed the mean of the wrong-vertex time, $\langle t_{\rm corr}^{\rm WV} \rangle$, to float in our fits. To accurately model the collision background in the signal region, dominated by WV events, we must understand how the selection of a wrong vertex affects the timing distributions which dominates the signal region.

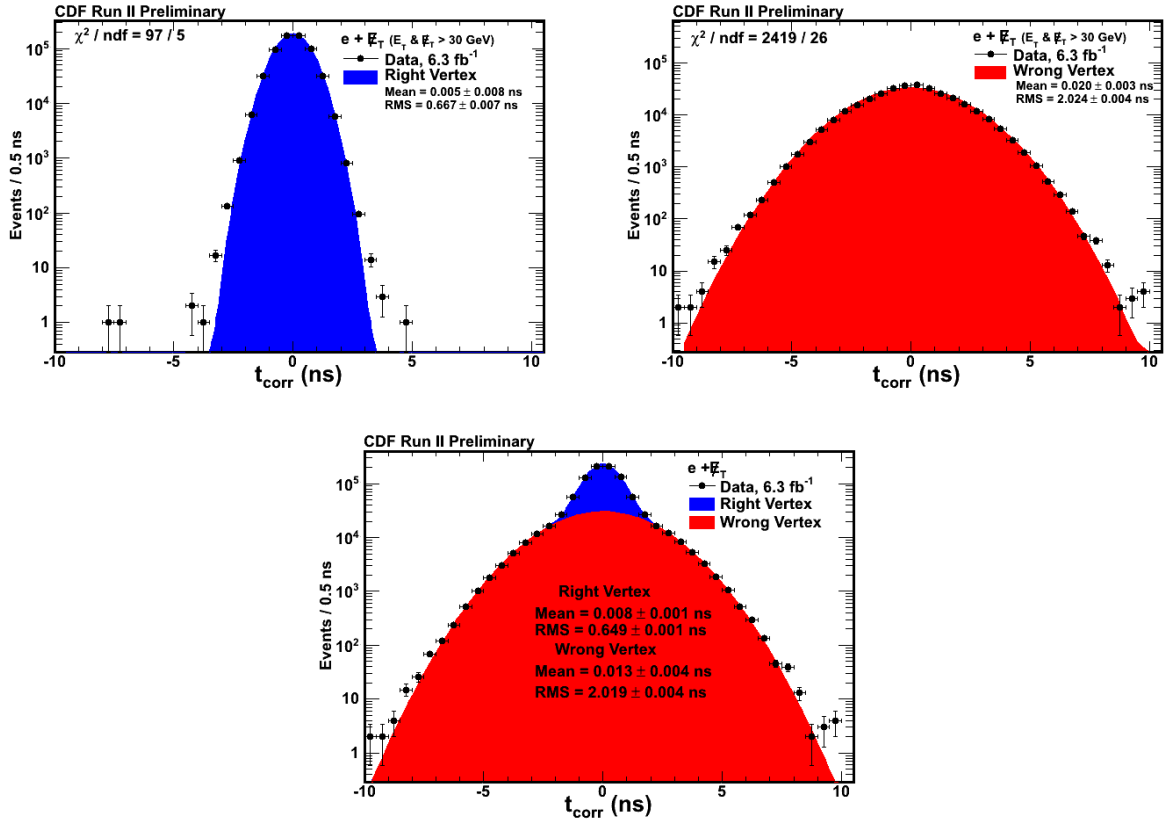

FIG. 4: (a): Right-vertex distribution for $e + \not\!\!E_{\rm T}$ in data. (b): Wrong-vertex distribution for $e + \not\!\!E_{\rm T}$ in data. (c): The $t_{\rm corr}$ distribution for $e + \not\!\!E_{\rm T}$ events where the electron track is ignored in the vertexing and the highest $\sum_{\rm tracks} p_{\rm T}$ vertex is always selected as is done for $\gamma + \not\!\!E_{\rm T}$ events. The red and blue show the best-fit result from the double-Gaussian fit even though we do not know whether it was a right vertex or a wrong vertex on an event-by-event basis. Note that the timing distribution is well-described by the two-Gaussian model.

The measured $t_{\rm corr}$ for a wrong vertex, $t_{\rm corr}^{\rm WV}$, is given by Eqn. 3, where the collision coordinate $(\vec{x}_{\rm i}, t_{\rm i})$ can be thought of as being randomly drawn from a collision distribution. Rewriting Eqs. 3 expressed specifically for wrong-vertex events we find

$$t_{\rm corr}^{\rm WV} = \left(t_f - t_i^{\rm WV}\right) - {\rm TOF}^{\rm WV} \tag{5}$$

where $t_{\rm i}^{\rm WV}$ is the time of the wrong-vertex collision and ${\rm TOF}^{\rm WV}$ is the incorrect time-of-flight assumption from the wrong vertex to the detected photon position and time in the calorimeter. However, the time of arrival, t_f, is given by the right vertex quantities

$$t_f = t_i^{\rm RV} + {\rm TOF}^{\rm RV} \tag{6}$$

where $t_{\rm i}^{\rm RV}$ is the time of the right-vertex collision and $\mathrm{TOF}^{\rm RV}$ is the time-of-flight from the vertex to $(\vec{x}_{\rm f}, t_{\rm f})$ in the calorimeter. So by substituting t_f from Eqn. 6 back into Eqn. 5, the corrected time for wrong-vertex events can be re-expressed as

$$t_{\rm corr}^{\rm WV} = \left(t_{\rm i}^{\rm RV} - t_{\rm i}^{\rm WV}\right) + \left(\mathrm{TOF}^{\rm RV} - \mathrm{TOF}^{\rm WV}\right) \tag{7}$$

The first term of Eqn. 7 describes the beam-collision times which are uncorrelated and both centered at zero. Thus, this term has a mean of zero but an RMS of $\sqrt{2} \cdot 1.28$ ns, where the 1.28 ns is the beam width of the collision from the beam parameters. The second term, $(\mathrm{TOF}^{\rm RV} - \mathrm{TOF}^{\rm WV})$, is a geometric effect, which we call the bias, which can shift $\langle t_{\rm corr}^{\rm WV} \rangle$ from zero by as much as a nanosecond. Any SM sources which produce events with a large value of this timing bias can produce many events in the signal region.

A second important thing to note about the bias term is that it has an RMS (typically 0.4 ns in our SM control samples) that is small compared to the RMS of the $\left(t_{\rm i}^{\rm RV} - t_{\rm i}^{\rm WV}\right)$ term. Thus, the combination of the terms in Eqn 7 produces a $t_{\rm corr}^{\rm WV}$ timing distribution which has an RMS determined by the first term (and is the same for all backgrounds, 2.0 ns), but a mean that is determined by the second term. Studies have shown that certain topologies can create events which are both very likely to have a wrong vertex selected and large values of the bias which are much larger on average. However, we have found ways to reject these events. Doing so is useful both because it reduces the overall event rate in the signal region and because without them large tails in this value could produce a $t_{\rm corr}^{\rm WV}$ distribution which is non-Gaussian at the high side, which makes background estimations more difficult.

Previous delayed photon analyses assumed that $\langle t_{\rm corr}^{\rm WV} \rangle = 0$ [3] and we now see why this is a bad assumption. Fig. 5 shows our control sample of $e + \not\!\!E_{\rm T}$ events where we remove the electron track from the vertexing and always choose the highest $\sum_{\rm tracks} p_{\rm T}$ vertex, but assume $\langle t_{\rm corr}^{\rm WV} \rangle = 0$ in our fit and fit in the region from [−7 ns, 2 ns]. We see that this grossly underestimates the number of events in the signal region and could be mistaken for a signal.

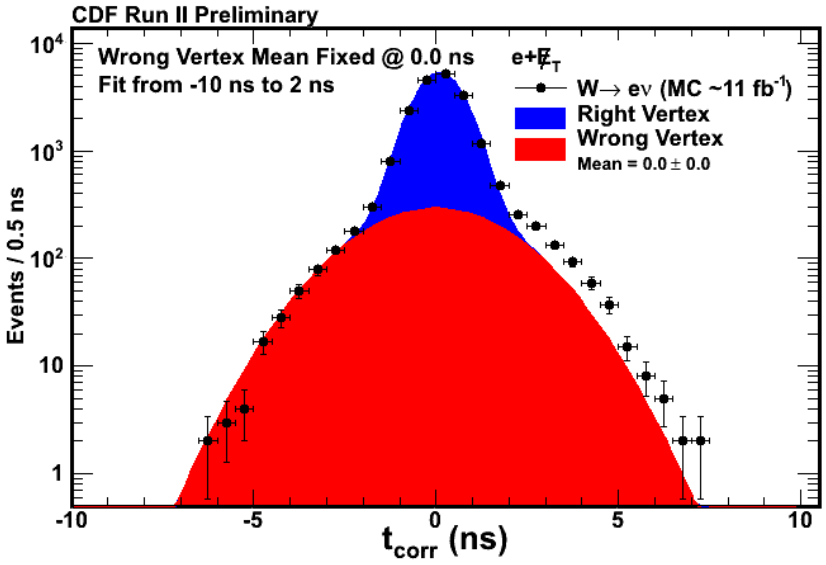

FIG. 5: The $t_{\rm corr}$ distribution for MC $W \to e\nu \to e + \not\!\!E_{\rm T}$ events with the wrong-vertex distribution mean fixed to 0.0 ns and the background rates determined from the fit to the data in the region [−7 ns, 2 ns] .

We next describe the effects which can produce large time events as well as our method for reducing the most biased events. After their reduction we are left with wrong-vertex backgrounds that are well-described by a Gaussian distribution which can be measured using data-driven techniques.

C. Sources of large bias SM Background and their Mitigation

Events with a wrong vertex are the dominant collision background in the signal region. There are a number of effects that shift the wrong-vertex mean time to values substantially greater than 0.0 ns, as well as produce anomalous events which would make the timing of wrong-vertex events deviate from Gaussian predictions. We next summarize

these effects and the cuts developed for reducing the most biased events. These cuts were listed in Table V. After a description of these cuts, we will describe the methods for measuring the remaining amount of bias in the next section.

1. *The Threshold Effect*

In most analyses, the photon $E_{\rm T}$ is defined as $E\sin\theta$ and θ is defined from the primary vertex in the event. However, it is always mismeasured in events that have selected a wrong vertex. An example of this is shown in Fig. 6 where the selection of the wrong vertex results in a shorter apparent path-length from the collision at $(\vec{x}_{\rm i}, t_{\rm i})$ to the calorimeter at $(\vec{x}_{\rm f}, t_{\rm f})$ than the true value. In this example, we have an event with a $\sin\theta_{\rm WV} > \sin\theta_{\rm RV}$, which means $E_{\rm T}^{\rm WV} > E_{\rm T}^{\rm RV}$. If $E_{\rm T}^{\rm RV} < 45$ GeV but $E_{\rm T}^{\rm WV} > 45$ GeV then this event will enter our sample. More importantly, the same geometry has ${\rm TOF}^{\rm RV} > {\rm TOF}^{\rm WV}$. It will have a value of $\left({\rm TOF}^{\rm RV} - {\rm TOF}^{\rm WV}\right)$ that is biased towards large times (i.e., $t_{\rm corr} > 0$ ns). Indeed, all events that enter the sample because of this selection bias will have a time that is biased towards $t_{\rm corr} > 0$. Similarly, if the selection of a wrong vertex causes an underestimate of $E_{\rm T}$, and causes the $E_{\rm T}$ value to decrease under the $E_{\rm T} > 45$ GeV threshold of the event selection, the event moves out of the sample. However, in this case $t_{\rm corr}^{\rm WV}$ is biased toward negative times and when negative-time events move out of the sample a positive time bias is also acquired. To minimize this event selection bias, we compute the photon $E_{\rm T}$ and $\not\!\!E_{\rm T}$ from the center of the detector ($z = 0$) instead of from the selected vertex, as this is the most common collision point and minimizes the average bias. These quantities are written as $E_{\rm T}^0$ and $\not\!\!E_{\rm T}^0$. Fig. 6(b) shows an MC sample of $W \to e\nu \to \gamma + \not\!\!E_{\rm T}$ events that pass the $E_{\rm T} > 25$ GeV and $E_{\rm T}^{\rm WV} > 45$ GeV cut as a function of their true $E_{\rm T}$. We see the large number of events that enter the sample and leave the sample and cause a large time bias in the final sample.

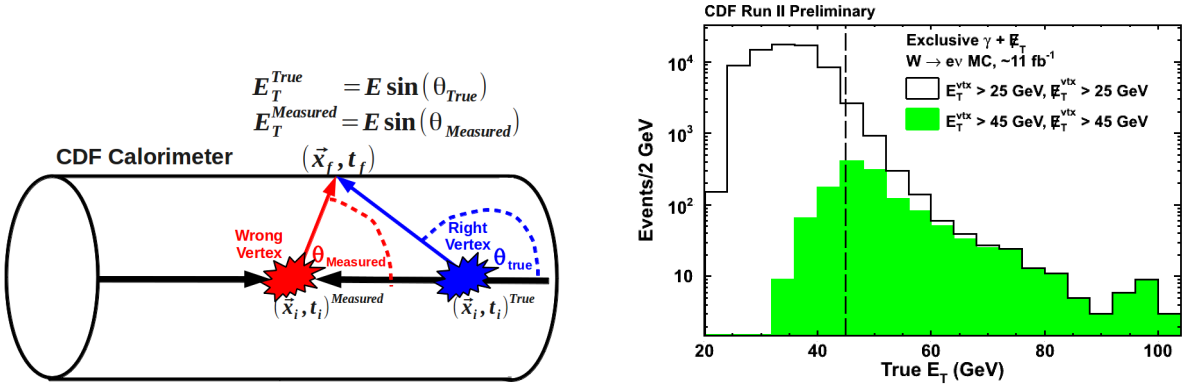

FIG. 6: (a): Both the $E_{\rm T}$ and the $t_{\rm corr}$ are mismeasured by choosing a wrong vertex. There is a high degree of correlation between the mismeasurements because picking a wrong vertex causes the apparent path length (${\rm TOF}^{\rm WV}$) to increase relative to the true path length (${\rm TOF}^{\rm RV}$), causing the measured corrected time and the measured $E_{\rm T}$ to both decrease. If picking a wrong vertex causes the apparent path length to decrease, the measured $t_{\rm corr}$ and the measured $E_{\rm T}$ both increase. (b): This shows the $E_{\rm T}$ distribution as measured around the true collision point for MC $W \to e\nu \to \gamma + \not\!\!E_{\rm T}$ with $E_{\rm T}^{\rm WV}$ greater than 25 GeV (white) and $E_{\rm T}^{\rm WV}$ greater than 45 GeV (green). The events to the left of the line at 45 GeV are those promoting over threshold. The difference between the white and the green above 45 GeV are those demoting below threshold. Both effects conspire to cause a net positive shift in the wrong-vertex distribution.

2. *Large $|z|$ Effect*

A second important effect is that any event that is produced with $|z| > 60$ cm will not have its collision identified as the selected vertex because of our SpaceTime vertex selection requirements in Table V. In this case, if the event does identify a SpaceTime vertex from an unrelated collision, we will always select the wrong vertex as well as have a positive (and potentially high) value of $({\rm TOF}^{\rm RV} - {\rm TOF}^{\rm WV})$. Standard model $\gamma +$ jet events are particularly sensitive to this effect because $|z| > 60$ cm increases the likelihood that the jet is not reconstructed, resulting in a $\gamma_{\rm delayed} + \not\!\!E_{\rm T}$ signature. Since the SM $\gamma +$ jet production cross section is relatively large, even a small fraction of the events having this type of production can produce a large number of $\gamma_{\rm delayed} + \not\!\!E_{\rm T}$ events. The true z position of collision, as

estimated using our $\gamma+$jet MC sample passing all the requirements in Table V, is shown in in Fig. 7. For this reason, we use the standard vertexing algorithm (described in detail in [24, 25]) which is more efficient at large $|z|$ to search for such collisions and reject any event containing a standard vertex with $|z| > 60$ cm. This cut is 95% efficient.

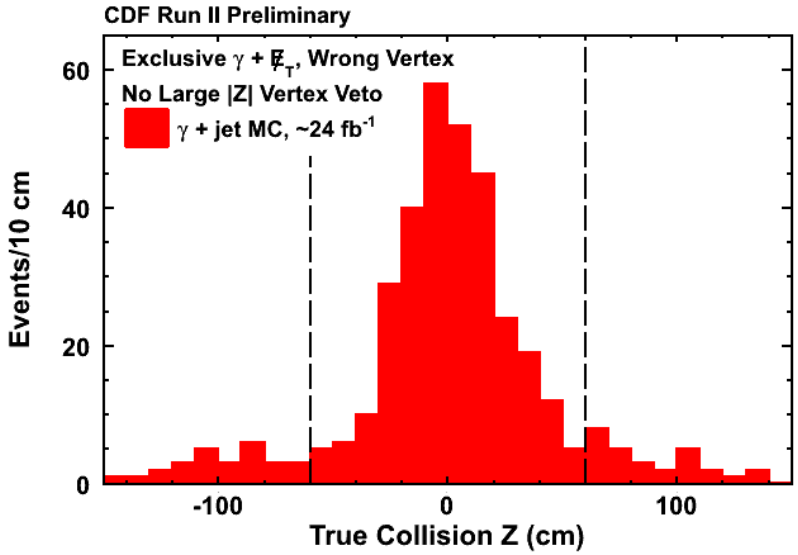

FIG. 7: The true collision position for a MC sample of $\gamma+$jet events that pass the final $\gamma+\not\!\!E_{\rm T}$ selection requirements. We note that a larger-than-average number of these events are produced with $|z| > 60$ cm because events that are produced at large $|z|$ have a higher probability that the orientation of the jet is directed outside of the detector than for events produced near the center of the detector. Because the primary vertex selection only considers SpaceTime vertices with $|z| < 60$ cm, all events with $|z| > 60$ cm have the wrong vertex selected and have large corrected values of $(\mathrm{TOF}^{\mathrm{RV}} - \mathrm{TOF}^{\mathrm{WV}})$. We reject events with evidence that there was a collision with $|z| > 60$ cm.

3. *Electrons Faking Photons*

Lastly, an important effect arises with $W \to e\nu \to \gamma_{\rm fake} + \not\!\!E_{\rm T}$ events where the electron is incorrectly identified as a photon. The longer the distance an electron travels from the collision point to the calorimeter face, the more likely they are to have a hard bremsstrahlung interaction inside the tracking material and create a falsely identified photon. Thus, $e \to \gamma_{\rm fake}$ candidates typically have a longer-than-average value of $\mathrm{TOF}^{\mathrm{RV}}$ as compared to promptly produced photons. Thus, photon candidates that originate as electrons have a bias towards larger arrival times (see Fig. 8), $\mathrm{TOF}^{\mathrm{RV}} > \mathrm{TOF}^{\mathrm{WV}}$. Detailed detector simulation studies show that this primarily occurs when the electron interacts with detector material, causing the electron to bremsstrahlung, emitting a photon. To remove $e \to \gamma_{\rm fake}$ candidates that pass the standard photon ID requirements, we reject any event that has a charged track which originates at the beam line with a similar pseudorapidity and azimuthal angle as the candidate photon (see Fig. 9) This requirement is 95% efficient and reduces the $W \to e\nu \to \gamma_{\rm fake} + \not\!\!E_{\rm T}$ by 70% in simulation, with comparable results in $Z \to ee \to e\gamma_{\rm fake}$ samples in data.

D. Summary of Background Sources in the Signal Region

After all the cuts listed in Table V, a study of the timing distributions for our backgrounds in our 8 control samples shows that the most biased types of events have been removed from our SM backgrounds, and each is well-described by a double-Gaussian distribution. A sample of results are shown in Fig. 10 where we see that the mean of each SM source can vary from ∼0.0 ns to 0.8 ns. Excellent agreement with modeling is seen. As expected, the small variation in the bias does not affect the RMS, and Fig. 10 shows that the RMS only varies within 2.0 ± 0.1 ns which we take as a systematic uncertainty. Studies have confirmed that combinations of these backgrounds shift the mean, but do not raise the RMS in a way that is significant compared to the 0.1 ns uncertainty. With this knowledge we can determine

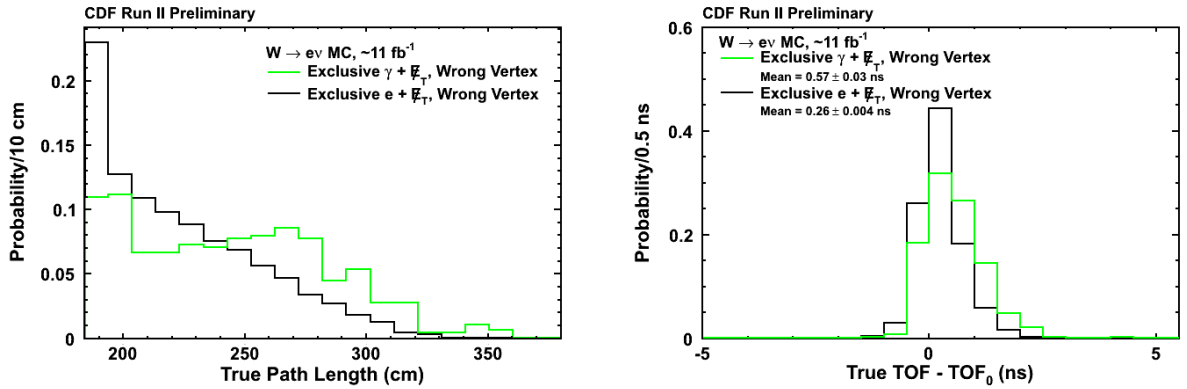

FIG. 8: A comparison of the average path length for $W \to e\nu$ events where the elctrons are reconstructed as electrons, and where they are reconstructed as photons. In (a) we show the full path length and in (b) we show the difference of the time of flight from the center of the detector which is a fixed point in space and effectively averages over all WV positions. In both cases, the path length is bigger for photons than fake electrons.

the amount of collision backgrounds in the signal region if we can measure the mean and normalization of the wrong-vertex backgrounds. The cosmics rate in the signal region can be estimated using standard techniques since beam halo and satellite backgrounds are negligible. With this understanding of the behavior of collision and non-collision backgrounds, we can proceed to the estimation techniques for predicting the final rate in the signal region.

A quantitave measure of the usefulness of the double Gaussian modeling is shown when we compare the number of events in the regions $[-7$ ns, -2 ns$]$ and $[2$ ns, 7 ns$]$ (labeled Wrong Vertex Sideband and Signal Region in Fig. 11) which are dominated by wrong-vertex events. Since the prediction for the ratio of events in these two regions is a simple integration of a Gaussian with a known width (assuming a mean), we can compare our background expectation method for the $\gamma_{\rm delayed} + \not\!\!E_{\rm T}$ signal region. Since we can measure the wrong-vertex mean of the timing distribution for MC, we can numerically integrate a Gaussian shape with RMS = 2.0 ns and 0.1 ns uncertainty to predict this ratio. The results are shown in Fig. 11(b) where the black line in Fig. 11(b) is not a fit, but is the prediction from the measured WV mean. The double Gaussian approximation does an excellent job of allowing us to predict the number of WV events in the signal region assuming we can measure the number of events in the sideband region and the mean of the WV distribution.

IV. BACKGROUND ESTIMATION METHODS

This analysis studies exclusive $\gamma_{\rm delayed} + \not\!\!E_{\rm T}$ events where the signal region is defined by the subset of photons in this sample having $2 < t_{\rm corr} < 7$ ns. The background expectation for this signal region has three components:

1. Right-vertex events: SM collision-based events for which the correct vertex was chosen. The shape of such events is known to be a Gaussian distribution whose mean is consistent with $t_{\rm corr} = 0 \pm 0.05$ ns and has an RMS of 0.65 ± 0.05 ns.

2. Wrong-vertex events: SM collision-based events for which the incorrect vertex was chosen. This happens when a vertex that was not the highest $\sum_{\rm tracks} p_T$ vertex produces the detected photon. The shape of such events is known to be a Gaussian distribution with a mean that can be significantly greater than zero ($\langle t_{\rm corr}^{\rm WV} \rangle > 0$ ns) because of several aforementioned detector effects. The RMS, however, remains consistently 2.0 ± 0.1 ns after all the selection requirements.

3. Cosmic Rays: Cosmics rays inherently produce a $\gamma + \not\!\!E_{\rm T}$ signature in the detector in a manner that is completely uncorrelated with the timing of beam collisions. While the rate of cosmic ray events producing the $\gamma + \not\!\!E_{\rm T}$ final state is large, since that rate is independent of the collision time, they are well-described by a uniform distribution in $t_{\rm corr}$.

As such, the background expectation for the exclusive $\gamma_{\rm delayed} + \not\!\!E_{\rm T}$ signal region is the sum of two Gaussian distributions and one uniform distribution (Fig. 4(d))–e.g. seven parameters are necessary to fully model the background. These parameters can be determined solely in a data-driven manner. While the $t_{\rm corr}$ distribution from the $\gamma + \not\!\!E_{\rm T}$ data

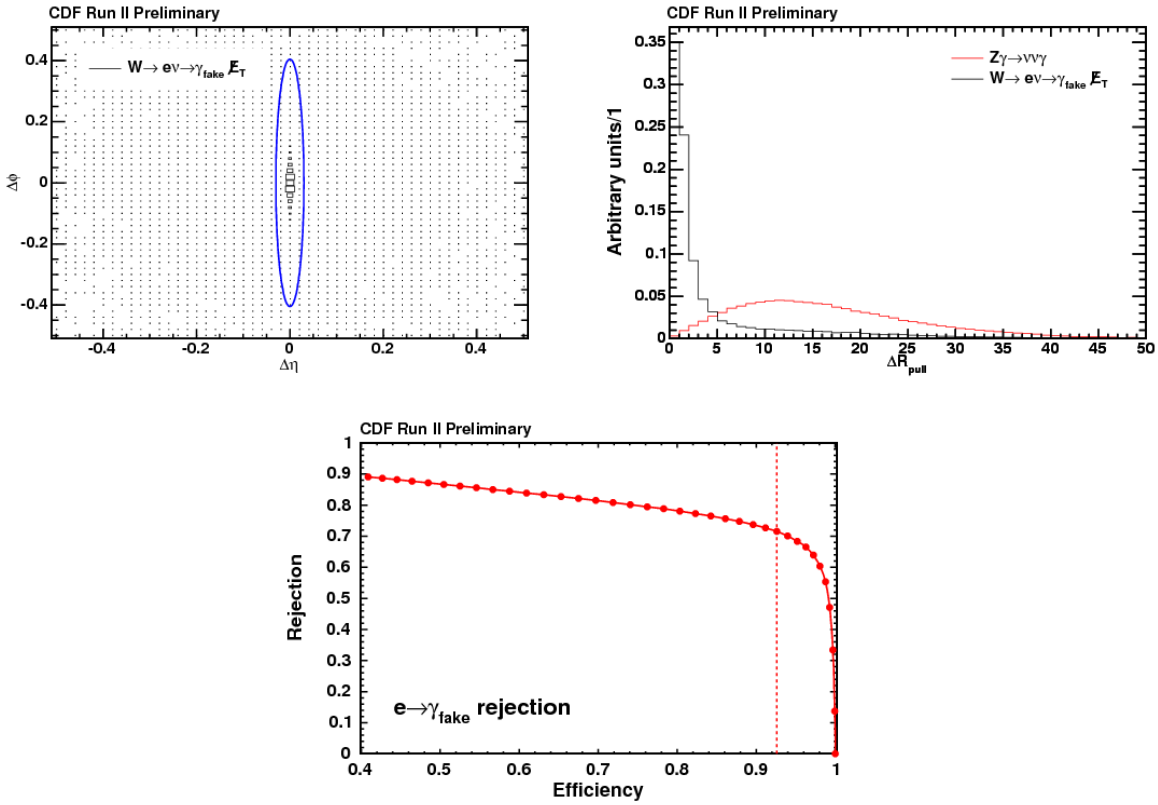

FIG. 9: Some plots showing the new $e \to \gamma_{\rm fake}$ rejection techniques used in this analysis. (a): The $\Delta\phi$ vs. $\Delta\eta$ (between the reconstructed photon and the closest track, for both variables) for the MC $W \to e\nu \to \gamma_{\rm fake} + \not\!\!E_{\rm T}$ sample. The oval indicates the $\Delta R_{\rm pull} > 5$ cut. (b): The closest track-photon distributions in $\Delta R_{\rm pull}$ for the control sample and the sample of fake-photon events. Making a cut on $\Delta R_{\rm pull}$ provides a better MC $Z\gamma \to \nu\nu\gamma \to \gamma + \not\!\!E_{\rm T}$ efficiency and $e \to \gamma_{\rm fake}$ rejection power than cutting on ΔR. Note that both samples are set to the same normalization. (c): The efficiency and rejection power of our cut as a function of the $\Delta R_{\rm pull}$ cut. Note that a cut at $\Delta R_{\rm pull} > 5$ (red dashed line) results in approximately 95% efficiency of MC $Z\gamma \to \nu\nu\gamma \to \gamma + \not\!\!E_{\rm T}$ and 73% rejection of $e \to \gamma_{\rm fake}$ candidates.

in the regions $-7 < t_{\rm corr} < 2$ ns and $20 < t_{\rm corr} < 80$ ns can be used to estimate six out of the seven parameters, more information is needed to estimate the wrong-vertex mean with an accuracy needed to be sensitive to new physics.

A. Using Events with No Reconstructed Vertex to Estimate $\langle t^{\rm WV}_{\rm corr} \rangle$

Accurate modeling of the wrong-vertex contribution to the signal region requires knowledge of $\langle t^{\rm WV}_{\rm corr} \rangle$. We have found that $\langle t^{\rm WV}_{\rm corr} \rangle$ can be estimated using a similiar, but orthogonal, sample of events passing the same $\gamma + \not\!\!E_{\rm T}$ selection requirements given in Tab. V, but requiring the events to have zero identified spacetime vertices. These events are topologically similar because many of the events with a wrong vertex often do not have the right vertex reconstructed; we will test this assumption with our eight control samples.

We define a new timing variable for the no-vertex sample:

$$t^0_{\rm corr} = t_f - t^0_i - {\rm TOF}^0 \tag{8}$$

where t^0_i is the average time of the collisions, which is zero so we set $t^0_i = 0$, and ${\rm TOF}^0$ is the time-of-flight from the average position of the collision which is in the center of the detector; i.e. $\vec{x}_i = 0$ in Eqn. 2. Rewriting we find

$$t_{\rm corr} = t^0_{\rm corr} - t_i - ({\rm TOF}^{\rm RV} - {\rm TOF}^0) \tag{9}$$

and

$$t^{\rm WV}_{\rm corr} = (t^{\rm RV}_i - t^{\rm WV}_i) + ({\rm TOF}^{\rm RV} - {\rm TOF}^{\rm WV}) \tag{10}$$

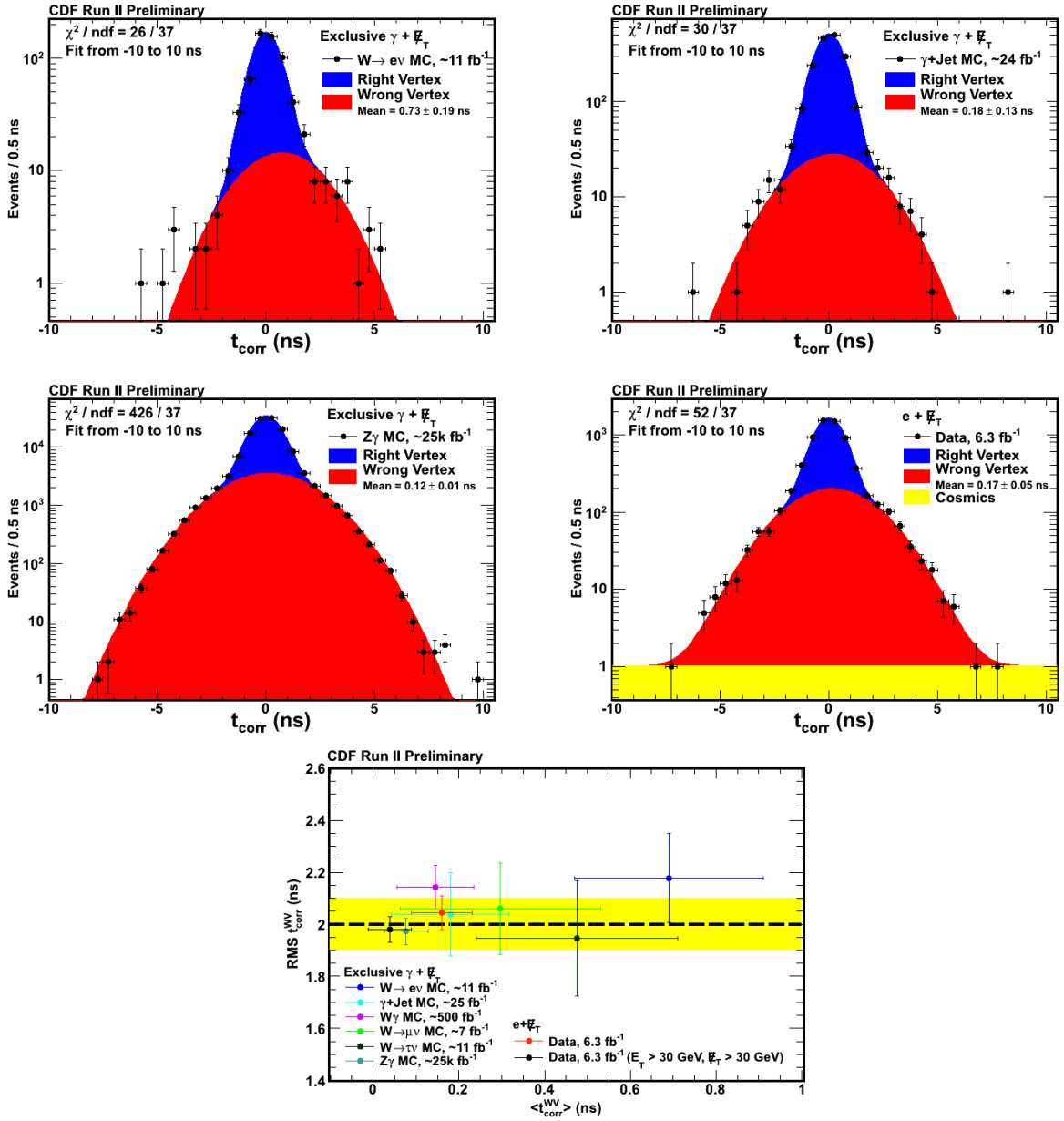

FIG. 10: Double Gaussian fits to some of the MC background and data $e + \not\!\!E_{\rm T}$ samples. (a): MC $W \to e\nu \to \gamma_{\rm fale} + \not\!\!E_{\rm T}$ (b): MC $\gamma +$ jets (c): MC $Z\gamma$ (d): data $e + \not\!\!E_{\rm T}$ (e): RMS vs. Mean of the wrong vertex distribution

Or better yet,

$$t_{\rm corr}^{\rm WV} = (t_i^{\rm RV} - t_i^{\rm WV}) + ({\rm TOF}^0 - {\rm TOF}^{\rm WV}) + ({\rm TOF}^{\rm RV} - {\rm TOF}^0) \tag{11}$$

where we have added and subtracted a $\rm TOF^0$ term for reasons that will be made clear in a moment.

We note that $\rm TOF^{RV} - TOF^0$ is a good measure of the average bias of the sample and is a purely geometric term that is sample dependent but does not depend on the WV in the event. It is identical for both collision and non-collision events. The final term, $({\rm TOF}^0 - {\rm TOF}^{\rm WV})$, only depends on the WV in the event, if any. Studies show that $\langle {\rm TOF}^0 - {\rm TOF}^{\rm WV} \rangle$ is close to zero with a small RMS for geometric reasons as shown in Fig. 12(a).

Based on this argument, we see that $\langle t_{\rm corr}^0 \rangle$ should be equal to $\langle t_{\rm corr}^{\rm WV} \rangle$ to a good degree of approximation, and has the advantage that $\langle t_{\rm corr}^0 \rangle$ can be measured with our no-vertex sample. This assumption is validated in our eight contral MC and data samples. Figure 12 compares the measured values of $\langle t_{\rm corr}^{\rm WV} \rangle$ vs. $\langle t_{\rm corr}^0 \rangle$. The former is something

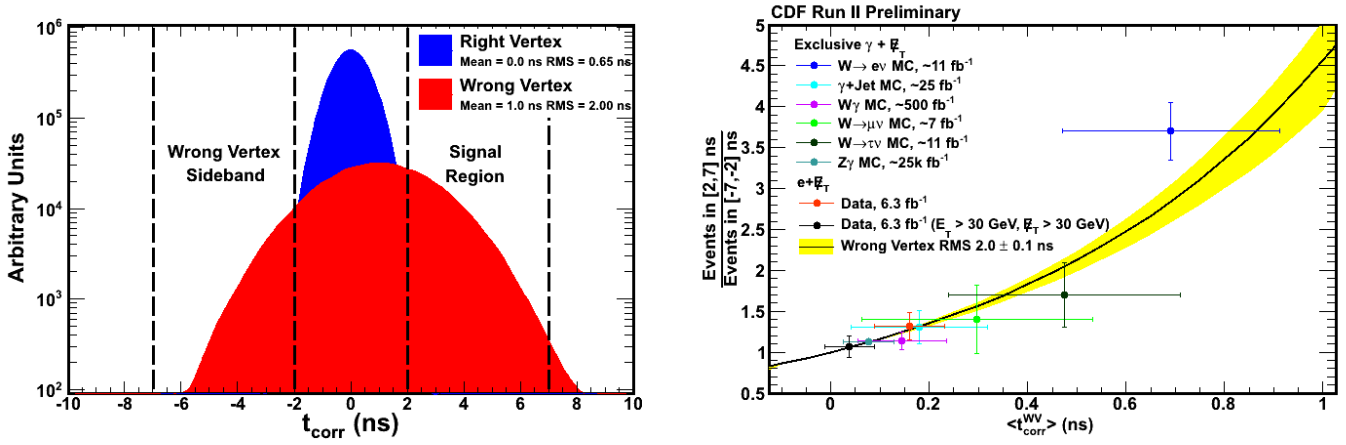

FIG. 11: (a): Wrong-Vertex sideband region and signal region. (b): The ratio of N(signal region) to N(wrong-vertex sideband region) vs. the fitted wrong-vertex mean for our eight control samples. We find that all samples agree well with the prediction from the double Gaussian approximation for a wide range of wrong-vertex means. (MC and two electron datasets)

we can measure only in our control samples (since we can use generator information in the MC or the electron track to identify the correct vertex), but the latter is something we can measure with data in the no-vertex sample. We take the systematic uncertainty on using this method to be 80 ps, i.e., $\langle t^{\rm WV}_{\rm corr}\rangle = \langle t^{0}_{\rm corr}\rangle \pm 80$ ps. Table X summarizes the mean and RMS results of a Gaussian distribution fit to events of the listed samples and we note that the RMS is 1.6 ns on average and does not vary much from sample to sample. We take 1.6 ± 0.1 ns as our systematic uncertainty. Figure 12 illustrates this by confirming that the RMS of the no-vertex sample is consistently 1.6 ns, regardless of the no-vertex mean of the sample. This direct correspondence between exclusive $\gamma + \not\!\!E_{\rm T}$ events that do and do not have an identified vertex means that all information necessary to model the expectation of the signal region can be obtained in a data-driven manner.

The most important test of our method is to use the measured value of $\langle t^{0}_{\rm corr}\rangle$ from our no-vertex sample to predict the ratio of events in the signal region to the control region in each of our MC and data control samples as if they were real data. Again, excellent agreement is observed as shown in Fig. 12(d). With this no-vertex data sample, we are able to estimate $\langle t^{\rm WV}_{\rm corr}\rangle$, which gives us the last piece of information we need to estimate the number of background events in the signal region.

Monte Carlo Sample	**Wrong Vertex Mean (ns)**	**Wrong Vertex RMS (ns)**
W$\to e\nu$	0.69 ± 0.22	2.18 ± 0.17
γ+Jet	0.18 ± 0.13	2.04 ± 0.16
Zγ	0.08 ± 0.05	1.97 ± 0.05
W$\to \mu\nu$	0.30 ± 0.23	2.06 ± 0.18
W$\to \tau\nu$	0.48 ± 0.22	1.97 ± 0.22
Wγ	0.14 ± 0.09	2.14 ± 0.08
$e + \not\!\!E_{\rm T}$ data	0.16 ± 0.07	2.05 ± 0.07
$e + \not\!\!E_{\rm T}$ data ($E^0_T > 30$ GeV and $\not\!\!E^0_{\rm T} > 30$ GeV)	0.04 ± 0.05	1.98 ± 0.05

TABLE IX: Summary of the measured mean $\langle t^{\rm WV}_{\rm corr}\rangle$ and RMS of the wrong vertex timing distributions for our SM MC and $e + \not\!\!E_{\rm T}$ data control samples selected using the cuts in Tables V and VIII. In these results we have allowed the mean and RMS of the WV Gaussian to float in the fit.

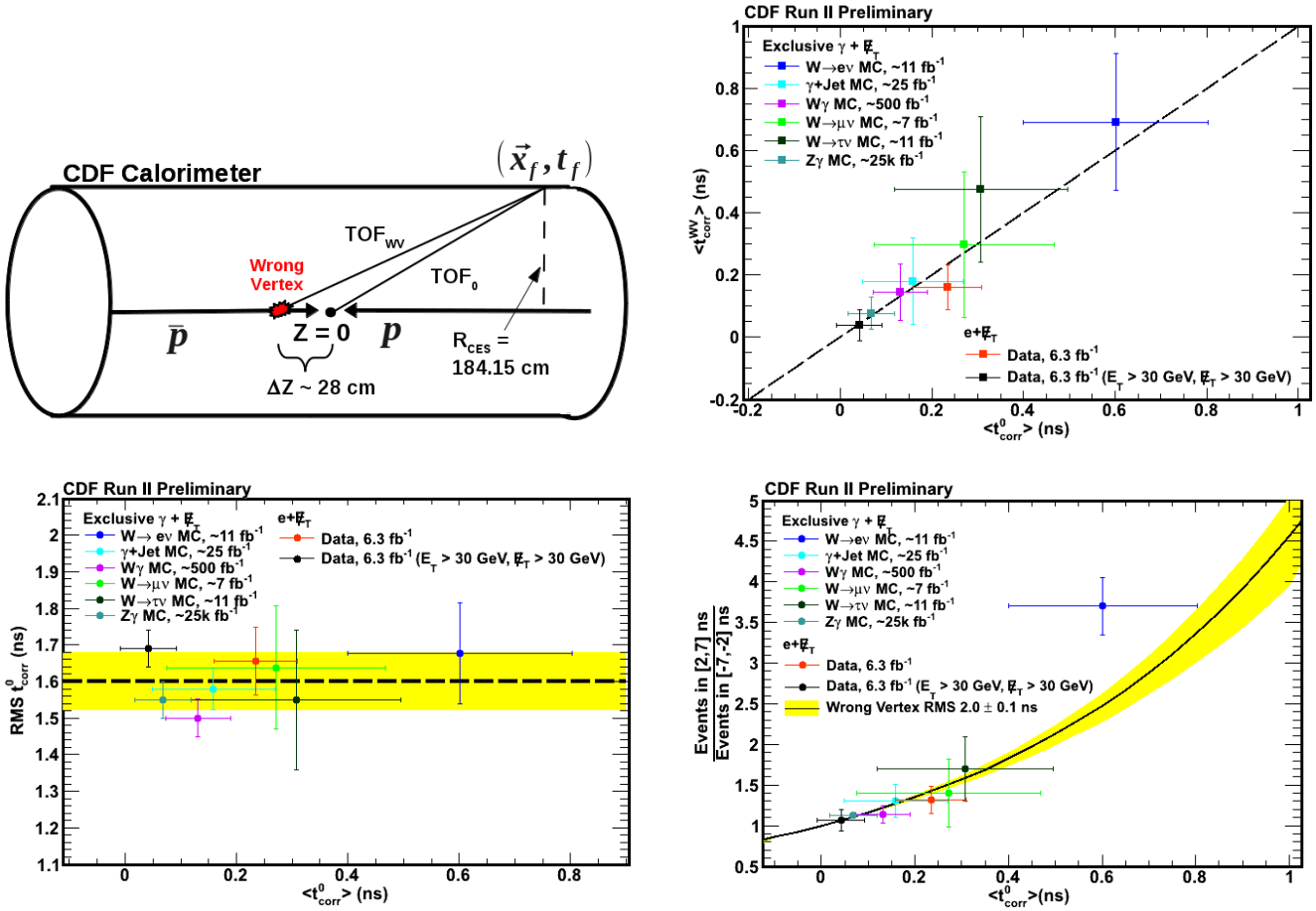

FIG. 12: For a number of MC datasets as well as two electron datasets from data, we isolate wrong-vertex (using generator quantities or the electron track) and no-vertex events. (a): If the characteristics of the true collisions are similar for wrong and no-vertex events, on average, the no-vertex and wrong-vertex times differ only by a small geometrical factor in their times-of-flight. (b): The fitted wrong-vertex mean vs. the fitted no-vertex mean. We find that the wrong-vertex and no-vertex means agree for all samples within a small systematic uncertainty. (c): The fitted no-vertex RMS vs. the fitted no-vertex mean for our 8 control datasets. We find that the no-vertex RMS is consistent with the assumption of 1.6 ns for all samples, regardless of the fitted no-vertex mean. (d): The no-vertex mean is an excellent predictor of the N(signal region)/N(wrong-vertex sideband) ratio as the wrong-vertex mean. Note that the line is not a fit, but rather the integrated ratio from the Gaussian assumption using the mean from the x-axis.

Monte Carlo Sample	No Vertex Mean (ns)	No Vertex RMS (ns)
W→ eν MC	0.61 ± 0.20	1.68 ± 0.14
γ+Jet MC	0.16 ± 0.11	1.58 ± 0.06
Zγ MC	0.07 ± 0.05	1.55 ± 0.05
W→ μν MC	0.27 ± 0.20	1.64 ± 0.17
W→ τν MC	0.31 ± 0.19	1.56 ± 0.19
Wγ MC	0.13 ± 0.06	1.50 ± 0.05
$e + \not\!\!E_T$ data	0.23 ± 0.08	1.66 ± 0.09
$e + \not\!\!E_T$ data ($E_T^0 > 30$ GeV and $\not\!\!E_T^0 > 30$ GeV)	0.04 ± 0.05	1.69 ± 0.05

TABLE X: Summary of the measured mean $\langle t^0_{\rm corr}\rangle$ and RMS of the no vertex timing distributions for our SM MC and $e + \not\!\!E_T$ data control samples selected using the cuts in Tables V and VIII. In these results we have allowed the mean and RMS of the Gaussians to float in the fit.

B. Sideband Regions for the Exclusive $\gamma_{\text{delayed}} + \not{E}_{\text{T}}$ Data

This analysis uses four sideband regions to estimate the expected number of background events in the signal region:

- Good-Vertex Collision Sideband: The sample of events passing the requirements in Tab. V with at least one identified spacetime vertex and $-7 < t_{\text{corr}} < 2$ ns. This sample is dominated by right and wrong vertex events, but has a large contribution from cosmics. After cosmics subtraction, this region will provide the normalization information for the two Gaussian distributions, and a little information about the WV mean.
- Good-Vertex Cosmic Ray Sideband: The sample of events passing the requirements in Tab. V with at least one identified vertex and $20 < t_{\text{corr}} < 80$ ns. This is a pure sample of cosmic ray events and provides the normalization for the uniform cosmic ray distribution in the signal and sideband regions for good vertex events.
- No-Vertex Collision Sideband: The sample of events passing the requirements in Tab. V, except with no identified spacetime vertices and $-3.5 < t^0_{\text{corr}} < 3.5$ ns. This sample is topologically equivalent to the wrong-vertex sample, but also has a cosmics contribution. The mean of this sample will be used to determine $\langle t^0_{\text{corr}} \rangle$, which will in turn be used to estimate $\langle t^{\text{WV}}_{\text{corr}} \rangle$.
- No-Vertex Cosmic Ray Sideband: The sample of events passing the requirements in Tab. V except with no identified space-time vertices and $20 < t^0_{\text{corr}} < 80$ ns. This sample is a pure sample of cosmic ray events and provides the normalization for the uniform cosmic ray distribution in the no-vertex collision sideband.

C. Systematic Uncertainties

The systematic uncertainties pertaining to this data-driven approach are summarized in Tab. XI. The uncertainty on $\langle t^{\text{RV}}_{\text{corr}} \rangle$ and RMS $\langle t^{\text{RV}}_{\text{corr}} \rangle$ are due to the tolerance of our timing calibration of the EMTiming and COT systems. The uncertainty on RMS $\langle t^{\text{WV}}_{\text{corr}} \rangle$ is derived from the observed variations between samples as well as variations due to combining wrong-vertex distributions with very different means.

Parameter	**Nominal Value**	**Systematic Uncertainty**
$\langle t^{\text{RV}}_{\text{corr}} \rangle$	0 ns	0.05 ns
RMS$\langle t^{\text{RV}}_{\text{corr}} \rangle$	0.65 ns	0.05 ns
$\langle t^{\text{WV}}_{\text{corr}} \rangle$	$\langle t^0_{\text{corr}} \rangle$	0.08 ns
RMS$\langle t^{\text{WV}}_{\text{corr}} \rangle$	2.0 ns	0.1 ns

TABLE XI: Systematic uncertainty constraint terms for the likelihood fit.

D. Data-Driven Likelihood Fit Method

This analysis uses a maximum likelihood method with a binned, extended likelihood function. In practice, the negative log likelihood is minimized:

$$-\ln \mathcal{L} \equiv \sum_i -n_i \ln \nu_i + \nu_i \tag{12}$$

where the sum is over t_{corr} bins of all the sideband regions, n_i is the observed number of events in bin i, and ν_i is the expected number of events in bin i. The shape for sideband regions in the sample with at least one identified vertex is governed by the double-Gaussian plus uniform distribution model described above while the shape for sideband regions in the sample with no vertices is governed by a single-Gaussian plus uniform distribution model.

A Gaussian constraint term is appended to Eqn. 12 to require the wrong-vertex mean to be constrained to the no-vertex mean within its uncertainty. Gaussian nuisance parameter terms are also appended to Eqn. 12 to account for systematic uncertainties. The fully combined and constrained negative log likelihood form is then:

$$-\ln \mathcal{L} \equiv -\ln \mathcal{L}_{\text{GV}} - \ln \mathcal{L}_{\text{NV}} - \sum_{\text{constraints}} \frac{(\alpha_k - \hat{\alpha}_k)^2}{2\sigma_k^2} \tag{13}$$

where $-\ln \mathcal{L}_{\text{GV}}$ is summed over the bins of good-vertex sidebands ($t_{\text{corr}} \in [-7,\ 2] \cup [20,\ 80]$ ns), $-\ln \mathcal{L}_{\text{NV}}$ is summed of the bins of no-vertex sidebands ($t_{\text{corr}} \in [-3.5,\ 3.5] \cup [20,\ 80]$ ns), α_k are the constrained parameters and $\hat{\alpha}_k$ are their nominal values. The systematic uncertainties on those parameters (σ_k) are listed in Tab. XI.

E. Sideband Results from Data and Final Expectations Using Pseudoexperiments

The data and the best-fit values for the no-vertex and good-vertex sideband samples in the data are shown in Fig. 13. It finds a mean wrong-vertex time of 0.20 ± 0.13 ns.

While many validation studies are done with our fitting methods on each of the control samples and agree with expectations, Fig. 14 illustrates results from validation studies with different sets of pseudoexperiments on the likelihood fit procedure in the most difficult scenario: with mixed factions of $W \to e\nu$, $Z\gamma \to \gamma + \not\!\!E_{\rm T}$ and $\gamma +$ jet events from MC. This choice more than covers the expected potential variation in WV means. The pull distribution, $\frac{(N_{\rm exp} - N_{\rm obs})}{\sigma_{\rm tot.}}$, for each of the pseudoexperiments shows a mean of zero and an RMS of less than 1.0 showing that the full set of analysis methods are unbiased and the uncertainties are well-estimated. While the fit method is shown to work for all values of $\langle t_{\rm corr}^{\rm WV} \rangle$ for our measured value and the number of cosmics and collision events, we expect an uncertainty of approximately 25 events on the number of background events in the signal region. We are now ready to open the box.

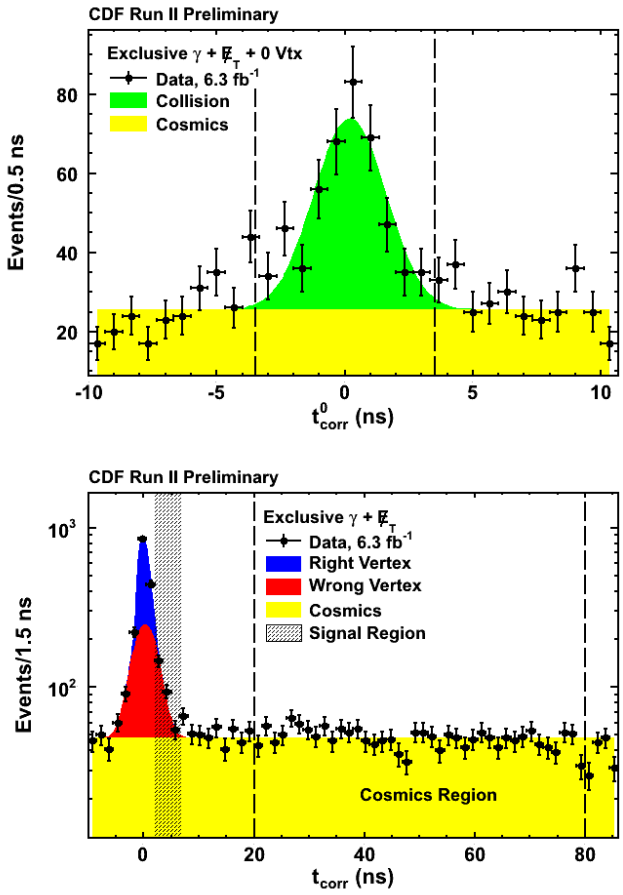

FIG. 13: These figures show the $t^0_{\rm corr}$ and $t_{\rm corr}$ distributions for the no-vertex and good-vertex sideband samples along with the best estimate from our fitting procedure. The signal region is blinded and our estimate comes from the sideband regions only.

V. RESULTS AND CONCLUSIONS

The final data result is shown in Fig. 15(a). Integrating over all sources of background, the method predicts 286 ± 24 events for the signal region ($2 < t_{\rm corr} < 7$ ns), whereas 322 events are observed. The full results are summarized in Tab. XII. The background contributions come from 159 ± 4 from cosmics, 126 ± 24 from wrong vertex, and 1.0 ± 0.6 from right vertex. Fig. 15(b) shows a plot of the data after a background subtraction. While most of the bins are above the expectations in the signal region, as would be expected for a new signal, we simply report the result from

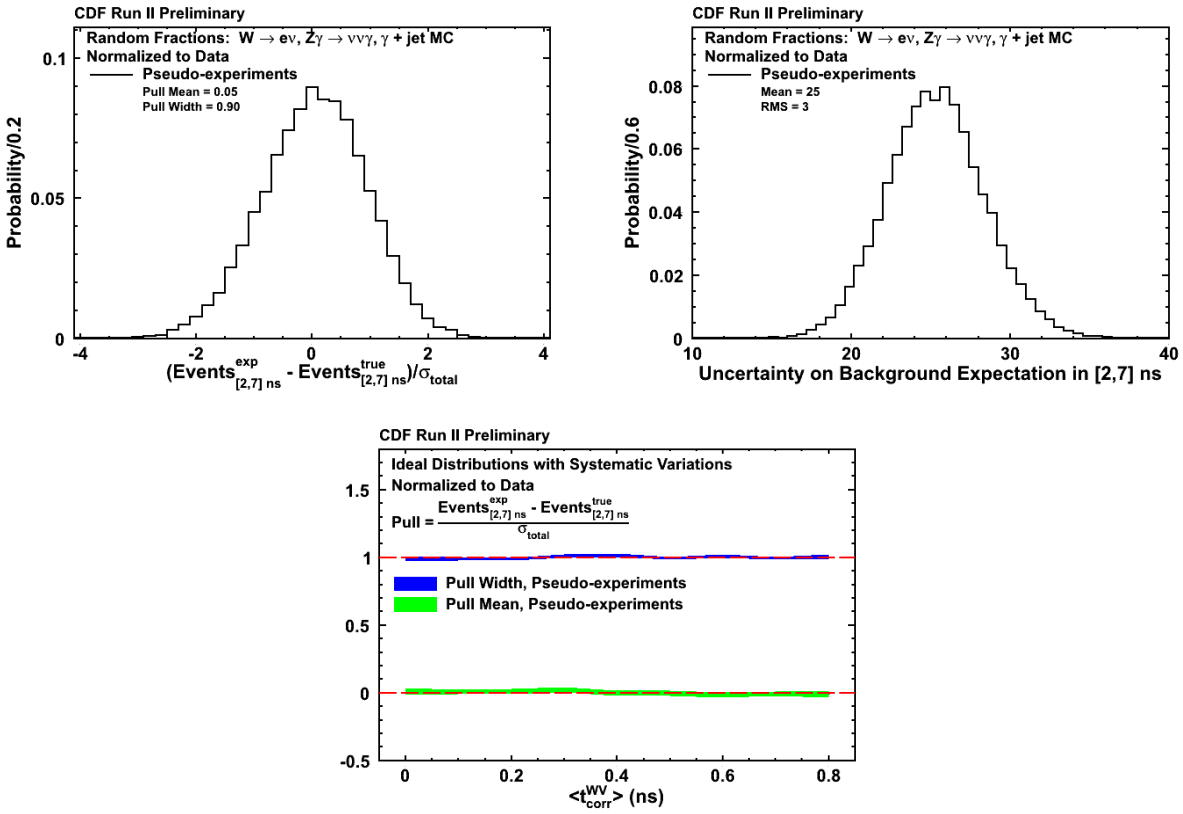

FIG. 14: The likelihood methods predict the number of events in the signal region for our pseudoexperiments as well as their uncertainty. Figure (a) shows the pull distribution for pseudoexperiments generated using MC datasets with varying amounts of $W \to e\nu$, $Z\gamma \to \nu\nu\gamma$ and $\gamma +$ jet events that pass the final $\gamma + \not\!\!E_{\rm T}$ requirements. The pull distribution has a mean very close to zero, which indicates a lack of bias. It has an RMS very close to 1, which indicates that the fit uncertainty is well estimated. (b): Uncertainty on background estimation (c): For generated wrong-vertex means from 0.0 ns to 0.8 ns, the fit remains unbiased and the uncertainties remain well estimated.

the counting experiment in the signal region. Accounting for the systematic and statistical uncertainties, this mild excess has a significance of 1.2 standard deviations above the expectation.

CDF Run II Preliminary $\int \mathcal{L} = 6.3$ fb^{-1}

	Signal $2 < t_{\rm corr} < 7$ **ns**	**RV Sideband** $-2 < t_{\rm corr} < 2$ **ns**	**WV Sideband** $-7 < t_{\rm corr} < -2$ **ns**
Right Vertex	1.0 ± 0.6	873 ± 65	0.6 ± 0.4
Wrong Vertex	126 ± 24	460 ± 60	89 ± 11
Cosmics	159 ± 4	128 ± 3	159 ± 4
Total Estimation	286 ± 24	1461 ± 38	249 ± 11
Data	322	1463	241

TABLE XII: The number of events predicted and observed in our three regions of interest. The total event expectations in the signal region is 286 ± 24; we observe 322 events in the data. This gives a modest 1.2σ excess. Note that the two sideband regions are determined using the fit, but are included here for completeness.

In conclusion, we have presented the first model-independent search for new physics in the exclusive $\gamma_{\rm delayed} + \not\!\!E_{\rm T}$ signature. Such a signature could show up in single Higgs production and decay into long-lived neutralinos in GMSB models. We have identified a number of new effects that can mimic the presence of new physics and reduced their impact on the analysis. After a set of requirements to both minimize such effects as well as account for them in our modeling, we observe 322 events on a background of 286 ± 24. While there is no evidence for new physics, we quantify our result using the sample counting experiment as having a modest excess with a significance of 1.2σ.

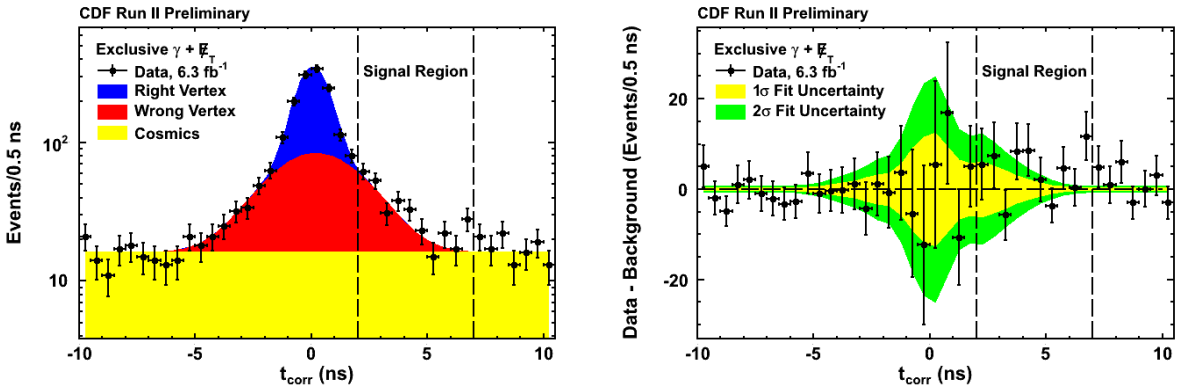

FIG. 15: (a): The final $t_{\rm corr}$ distribution for our data sample along with the best fit values of the backgrounds from timing distributions for right vertex, wrong vertex, and cosmics as function of $t_{\rm corr}$. (b): Results with expected backgrounds subtracted.

Acknowledgments

We thank the Fermilab staff and the technical staffs of the participating institutions for their vital contributions. This work was supported by the U.S. Department of Energy and National Science Foundation; the Italian Istituto Nazionale di Fisica Nucleare; the Ministry of Education, Culture, Sports, Science and Technology of Japan; the Natural Sciences and Engineering Research Council of Canada; the National Science Council of the Republic of China; the Swiss National Science Foundation; the A.P. Sloan Foundation; the Bundesministerium fuer Bildung und Forschung, Germany; the Korean Science and Engineering Foundation and the Korean Research Foundation; the Particle Physics and Astronomy Research Council and the Royal Society, UK; the Russian Foundation for Basic Research; the Comision Interministerial de Ciencia y Tecnologia, Spain; and in part by the European Community's Human Potential Programme under contract HPRN-CT-20002, Probe for New Physics.

[1] D. A. Toback and P. Wagner, Phys. Rev. **D 70**, 114032 (2004).
[2] J. D. Mason and D. Toback, Phys. Lett. **B 702**, 377 (2011).
[3] A. Abulencia *et al.* (CDF Collaboration), Phys. Rev. Lett. **99**, 121801 (2007).
[4] T. Aaltonen *et al.* (CDF Collaboration), Phys. Rev. **D 78**, 032015 (2008).
[5] B. Allanach *et al.*, Eur. Phys. J. **C 25**, 113 (2002).
[6] M. Abazov *et al.* (DØ Collaboration), Phys. Rev. Lett. **101**, 011601 (2008).
[7] A. Heister *et al.* (ALEPH Collaboration), Eur. Phys. J. **C** pp. 339–351 (2002).
[8] S. Chatrchyan *et al.* (CMS Collaboration), Phys. Rev. Lett. **106**, 211802 (2011).
[9] M. Gataullin, S. Rosier, L. Xia, and H. Yang, AIP Conference Proceedings **903**, 217 (2007).
[10] G. Pasztor, PoS **HEP2005**, 346. 4 p (2005).
[11] J. Abdallah *et al.* (DELPHI Collaboration), Eur. Phys. J. **C 38**, 395 (2005).
[12] G. Aad *et al.* (ATLAS Collaboration), Phys. Rev. Lett. **106**, 121803 (2011).
[13] P. D. Acton *et al.*, Phys. Lett. **B 311**, 391 (1993).
[14] J. D. Mason, D. E. Morrissey, and D. Poland, Phys. Rev. **D 80**, 115015 (2009).
[15] T. Aaltonen *et al.* (CDF Collaboration), Phys. Rev. **D 82**, 052005 (2010).
[16] J. Asaadi, Ph.D. thesis, Texas A&M University, College Station, Texas (2012).
[17] A. Aurisano, Ph.D. thesis, Texas A&M University, College Station, Texas (2012).
[18] T. Aaltonen *et al.* (CDF Collaboration), Phys. Rev. Lett. **101**, 181602 (2008).
[19] A. Abulencia *et al.* (CDF Collaboration), J. Phys. **G**: Nucl. Part. Phys. **34**, 2457 (2007).
[20] In the CDF II detector, a particle's direction is characterized by the azimuthal angle ϕ, the pseudorapidity $\eta = -\ln[\tan(\theta/2)]$, and the polar angle θ measured with respect to the proton beam direction. The transverse energy E_T is defined as $E\sin\theta$, where E is the energy in the electromagnetic and hadronic calorimeter towers associated with a cluster of energy deposition. The cylindrical axis of the detector is denoted as the z coordinate and increases positively in the direction of the proton beam.
[21] M. Goncharov *et al.*, Nucl. Instrum. Meth. **565**, 543 (2006).
[22] D. Acosta *et al.* (CDF Collaboration), Phys. Rev. **D 71**, 031104 (2005).
[23] E. S. Lee, Ph.D. thesis, Texas A&M University, College Station, Texas (2010).
[24] B. Ashmanskas *et al.*, Nucl. Instrum. Meth. **518**, 532 (2004).
[25] W. Ashmanskas *et al.*, Nucl. Instrum. Meth. **477**, 451 (2002).
[26] T. Sjostrand *et al.*, Comput. Phys. Commun. **135**, 238 (2001).
[27] T. Sjostrand, S. Mrenna, and P. Skands, J. of High Energy Phys. **0605**, 026 (2006).
[28] U. Baur, T. Han, and J. Ohnemus, Phys. Rev. **D 57**, 2823 (1998).
[29] E. Gerchtein and M. Paulini (2003), arXiv:physics.comp-ph/0306031.
[30] T. Aaltonen *et al.* (CDF Collaboration), Phys. Rev. **D 77**, 112001 (2008).